ACS Catalysis

Research Article

pubs.acs.org/acscatalysis

Facile Route for Synthesizing Ordered Mesoporous Ni−Ce−Al Oxide Materials and Their Catalytic Performance for Methane Dry Reforming to Hydrogen and Syngas

Ning Wang,[†,‡] Kui Shen,[†] Lihong Huang,[§] Xiaopeng Yu,[‡] Weizhong Qian,*[,†] and Wei Chu*[,‡]

[†]Beijing Key Laboratory of Green Chemical Reaction Engineering and Technology, Department of Chemical Engineering, Tsinghua University, Beijing 100084, China

[‡]Department of Chemical Engineering, Sichuan University, Chengdu 610065, China

[§]Department of Chemical Engineering, Chengdu University of Technology, Chengdu 610059, China

ABSTRACT: A series of ordered mesoporous Ni−Ce−Al composite oxides with various cerium contents were synthesized via a one-pot route: evaporation-induced self-assembly (EISA) strategy and tested in methane dry reforming for hydrogen and synthesis gas production. Using this method, the hydrophobic nickel precursor was directly incorporated into the hydrophobic cores of surfactant micelles, and thus, the highly dispersed Ni nanoparticles were stabilized inside the mesopore channels of an alumina matrix. For comparison, Ni-based catalysts were also prepared by a traditional impregnation method. The characterization results confirmed that the ordered mesostructures were well maintained in all of the cerium-incorporated Ni−Al materials (Ce/(Ce + Al) molar ratio ≤ 3%). The catalyst with a Ce/(Ce + Al) ratio of 1% exhibited the highest catalytic activity (with CO_2 and CH_4 initial conversions being 70% and 68% at 700 °C, respectively) and remained stable in a methane dry reforming reaction. This improved activity can be attributed to the large surface area and high dispersion and reducibility of Ni nanoparticles, which were stable because of the stable alumina framework and high oxygen mobility in these cerium-containing samples. Resistance to carbon deposition was found over the Ni−Ce−Al catalyst, whereas amounts of graphitic carbon species were found over the Ni-impregnated catalysts, which was responsible for deactivation.

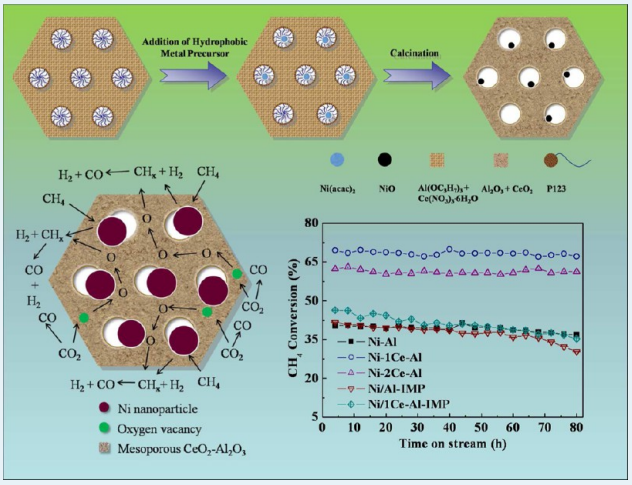

KEYWORDS: *One-pot synthesis, Ordered mesopores, Confinement effect, Methane dry reforming, Hydrogen*

1. INTRODUCTION

Carbon dioxide and methane are the main greenhouse gases that cause global climate change. Recently, extensive attention has been giben to control and utilization of these greenhouse gases.[1−4] Carbon dioxide reforming of methane or methane dry reforming is an efficient route for conversion of these two greenhouse gases into synthesis gas (syngas).[5−7] The produced syngas with a H_2/CO molar ratio around 1 is suitable to be transformed to valuable hydrocarbons through Fischer−Tropsch (F−T) synthesis and oxosynthesis.[8,9]

For catalysts in methane dry reforming, the noble metals, such as Rh, Ru, Pt, Pd, Ir, have presented considerable catalytic activity, but the high cost is a concern for industrial application.[10−14] Nickel-based catalysts have exhibited excellent catalytic activity for methane dry reforming, but they are reported to easily deactivate due to carbon deposition or sintering.[15,16] It has been reported that highly dispersed Ni particles can inhibit carbon deposition,[17−19] but these highly dispersed Ni species are easily agglomerated during the reaction.[20]

The confinement effect of mesopores can be a strategy to address this concern. Using supports with ordered mesoporous structure (for instance, ordered siliceous materials), the metal nanoparticles can be confined inside the pore channels of mesoporous materials, and thus, a high dispersion can be maintained and long-term stability is achieved.[21−23] Typically, monodispersed Ag nanoparticles over SBA-15 mesoporous materials have been prepared through an in situ autoreduction method.[24] The confinement of mesopores has resulted in an enhanced thermal stability of Ag nanoparticles inside the pore channels of SBA-15. In previous studies, Ni-based mesoporous materials, both mesoporous silica (SBA-15, MCM-41, TUD-1) and mesoporous metal oxide ($CaO−ZrO_2$, $La_2O_3−ZrO_2$,

Received: January 26, 2013
Revised: May 25, 2013
Published: June 24, 2013

   dx.doi.org/10.1021/cs4003113 | ACS Catal. 2013, 3, 1638−1651

Scheme 1. Schematic Diagram of the Nickel Nanoparticles/Mesoporous Alumina Preparation

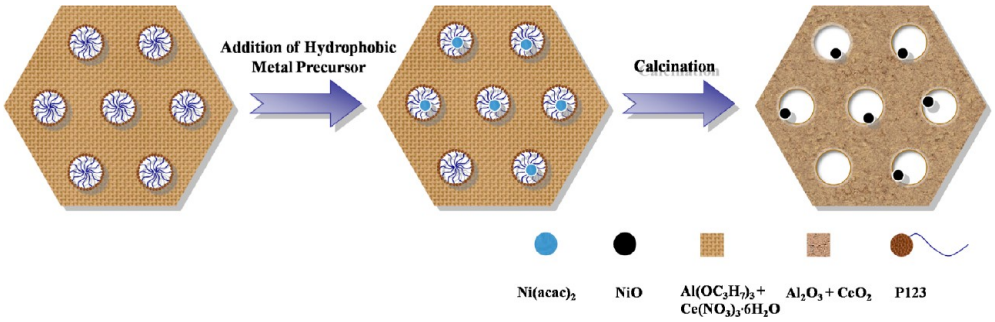

CeO_2–ZrO_2), have exhibited excellent catalytic behavior in methane dry reforming.[21−27]

In recent years, ordered mesoporous alumina has been widely applied in catalysts and adsorption because of its tunable pore size, large surface area, and high thermal stability.[28−30] Via a simple solvent evaporation-induced self-assembly (EISA) strategy, highly ordered mesoporous alumina with 2D hexagonal structure has been successfully synthesized by Yuan et al. and has showed a high thermal stability up to 1000 °C.[29] This reproducible route was used for the preparation of mesoporous materials, especially nonsiliceous mesoporous materials.[31] Because the active component can be confined in the channels of mesopores with some size limitation, ordered mesoporous alumina loaded with metal oxides has attracted much attention as new functional materials with excellent catalytic activity.[32,33] However, the traditional impregnation of mesoporous alumina with metal oxide precursors often leads to pore blockage or damage, which results in fast deactivation.

Herein, we have developed a simple one-pot synthesis route. This facile method is based on a sol−gel process combined with EISA in ethanol using Pluronic P123 as the template.[29,30] In the micellar solution of the alumina precursor, the hydrophobic Ni precursor could be directly incorporated into the inner hydrophobic cores of the surfactant micelles. After removing the template through calcination in air, the alumina formed a stable ordered mesoporous skeleton, and the Ni nanoparticles could be uniformly dispersed in the pore channels of the mesoporous alumina (Scheme 1).

In this study, a series of ordered mesoporous Ni−Al and Ni−Ce−Al oxide catalysts with different cerium contents were prepared via the one-pot EISA method. The cerium promoter could increase the oxygen mobility of the catalysts as well as the stability of metal particles.[34] Their catalytic behaviors in the methane dry reforming reaction were investigated and compared in detail with those of Ni-impregnated catalysts. The influence of the CeO_2 modifier and the deactivation aspect are also discussed.

2. EXPERIMENTAL SECTION

2.1. Preparations of Ni−Al and Ni−Ce−Al Catalysts. Ordered mesoporous Ni−Al and Ni−Ce−Al oxide catalysts was prepared via an improved one-pot EISA method based on the previously reported literature.[29,35,36] The Ni content was fixed at 7 wt % in all catalysts in this work, and the molar ratio of Ce/(Ce + Al) was 1%, 2%, 3%, and 4%.

In a typical synthesis procedure, $(EO)_{20}(PO)_{70}(EO)_{20}$ Triblock copolymer (Pluronic P123, typical M_n = 5800, Sigma−Aldrich) and an expected stoichiometric amount of $Ni(acac)_2$ were dissolved in 10 mL of anhydrous ethanol at room temperature (RT), then a solution containing 10 mL of ethanol, 1.7 mL of 67 wt % HNO_3, 2.04 g of $Al(OPr^i)_3$ (10 mmol), and different amounts of $Ce(NO_3)_2{\cdot}6H_2O$ was added into the above solution under vigorous stirring. The mixture was continuously stirred for 5 h and then placed in the oven at 60 °C for evaporation of EtOH for 48 h. The final gel was calcined at 700 °C for 4 h. The obtained sample was denoted as Ni−*x*Ce−Al, where *x* represents the Ce/(Ce + Al) molar percentage. The preparation of the ordered mesoporous Al_2O_3 and CeO_2−Al_2O_3 support materials was similar to that of the Ni−*x*Ce−Al catalysts without the addition of $Ni(acac)_2$.

The Ni-impregnated catalysts were prepared by an incipient impregnation method. The mesoporous Al_2O_3 and CeO_2−Al_2O_3 powder were mixed with the $Ni(NO_3)_2$ solution under magnetic stirring at 80 °C to achieve a 7 wt % loading amount. After stirring, the solution was dried and then calcined in air at 700 °C for 4 h. The samples were designated as Ni/Al-IMP and Ni/*x*Ce−Al-IMP, where *x* represents the Ce/(Ce + Al) molar percentage.

2.2. Catalyst Characterization. The X-ray diffraction patterns (XRD) were carried out on an X-ray diffraction apparatus (Philips X'pert PRO) with Cu Kα (45 kV, 50 mA) radiation.

The specific surface areas, total pore volume and average pore diameter were determined from N_2 adsorption/desorption isotherms at −196 °C using an automated surface area and pore size analyzer (Quadrasorb SI apparatus). Before each measurement, the sample was degassed in vacuum at 300 °C for 3 h.

The morphology of the materials was visualized using a JEOL JEM 2010 transmission electron microscope (TEM) operated at 120.0 kV. The samples were dispersed in ethanol assisted by an ultrasonic technique.

The X-ray photoelectron spectra (XPS) were recorded on an XSAM800 spectrometer with an Al Kα ($h\nu$ = 1486.6 eV) X-ray source. Charging effects were corrected by adjusting the binding energy of the C 1s peak from carbon contamination to 284.6 eV.

Temperature-programmed reduction (TPR) experiments were carried out in a fixed-bed reactor. Prior to the TPR measurements, samples were pretreated at 300 °C for 0.5 h in flowing Ar (50 mL/min) to remove any moisture and adsorbed impurities. After cooling the reactor to room temperature, the reduction gas of 4.2% H_2/N_2 at a flow rate of 30 mL/min was introduced. The temperature of the reactor was raised linearly to 900 °C at a rate of 10 °C/min by a temperature controller. The hydrogen consumption was analyzed online by a SC-200 gas chromatograph with a thermal conductivity detector (TCD).

dx.doi.org/10.1021/cs4003113 | ACS Catal. 2013, 3, 1638−1651

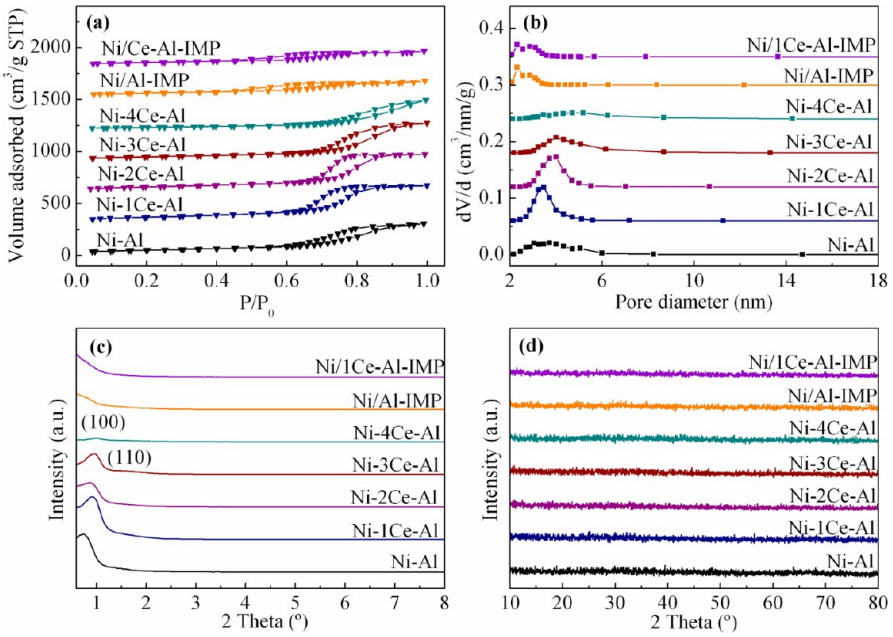

Figure 1. (a) Nitrogen adsorption−desorption isotherms, (b) pore size distributions, (c) low-angle XRD patterns, and (d) wide-angle XRD patterns of various samples.

Hydrogen chemisorption was performed in a static volume apparatus Autosorb-1-C (Quantachrome). The samples were first dried under He atmosphere at 250 °C for 2 h and reduced in purified H_2 at 700 °C for 1 h using a heating rate of 10 °C/min. The samples were purged with helium at this temperature for 2 h and then cooled in vacuum to 40 °C for the chemisorption measurement.

The amount of carbon deposited on the used samples was determined with a thermogravimetric analyzer (TGA Q500). The sample was heated in flowing air from room temperature to 800 °C at a heating rate of 10 °C/min.

The O_2 temperature-programmed desorption (O_2-TPD) experiments were carried out in a fixed-bed reactor. A 100 mg sample was pretreated with N_2 at 700 °C for 30 min, followed by O_2 adsorption at room temperature for 30 min. The sample was then purged with N_2 gas to remove the physically adsorbed O_2, followed by heating the sample from 50 to 950 °C at a linear heating rate of 10 °C/min in the N_2 flow. The effluent gases were analyzed online by a Hiden QIC-20 mass spectrometer.

Temperature-programmed hydrogenation (TPH) experiments were carried out in a fixed-bed reactor. A 100 mg sample after reaction was loaded, and the reaction gas of pure H_2 at a flow rate of 30 mL/min was introduced. The temperature of the reactor was raised linearly from 50 to 800 °C at a rate of 10 °C/min by a temperature controller. The products were analyzed online by a Hiden QIC-20 mass spectrometer.

2.3. CO_2 Reforming of Methane To Produce Hydrogen and Syngas. The catalytic activity measurements were carried out under atmospheric pressure using a continuous fixed-bed flow reactor. Typically, 100 mg of catalyst was loaded into the reactor using quartz wool. The molar ratio of CH_4 to CO_2 was 1:1, and GHSV was 36 000 mL/(h·g_{cat}). The catalyst was reduced in the reactor with H_2 at 700 °C for 1 h before the test. Effluent gases from the reactor were analyzed online by a GC-1690 model gas chromatograph with a TDX-01 column and a thermal conductivity detector (TCD).

3. RESULTS AND DISCUSSION

3.1. Catalyst Characterization. Figure 1a, b shows the nitrogen adsorption−desorption isotherms and the pore size distributions of the catalysts, respectively. The textural properties of various mesoporous catalysts are listed in Table 1. For the Ni−Al sample, the isotherm presented a typical type

Table 1. Textural Properties and Compositions of Various Samples

sample	S_{BET} (m^2/g)[a]	V_p (cm^3/g)[b]	D_p (nm)[c]	composition (wt %)[d] Ni	Ce
Ni−Al	208	0.47	3.7	6.82	0.00
Ni−1Ce−Al	245	0.58	3.7	7.76	2.31
Ni−2Ce−Al	212	0.58	4.0	7.12	4.45
Ni−3Ce−Al	173	0.58	4.0	7.33	6.84
Ni−4Ce−Al	115	0.46	5.2	7.37	8.92
Ni/Al-IMP	181	0.27	2.2	6.51	0.00
Ni/1Ce−Al-IMP	189	0.26	2.2	7.79	2.08

[a]BET specific areas. [b]Total pore volumes were obtained at P/P_0 = 0.99. [c]Average pore diameters were calculated by BJH method. [d]Ni and Ce contents were determined by EDX analysis.

IV curve with H1 shaped hysteresis loop, which was characteristic of mesopore materials with a "cylindrical-shaped" channel. The steepness of the capillary condensation step between P/P_0 = 0.65−0.85 implied the uniformity of mesopores in the framework. When cerium was incorporated into mesoporous Ni−Al, the shape of the type IV isotherm with a large H1 hysteresis loop still remained, illuminating a similar mesoporous structure in Ni−xCe−Al ($x \leq 3$). Moreover, compared with that of the Ni−Al sample, the isotherms for Ni−xCe−Al ($x \leq 3$) showed steeper and higher condensation. This suggested that more uniform mesopores and larger pore volumes were obtained with cerium modification.[30] Furthermore, with an increase in the cerium amount, the hysteresis

dx.doi.org/10.1021/cs4003113 | ACS Catal. 2013, 3, 1638−1651

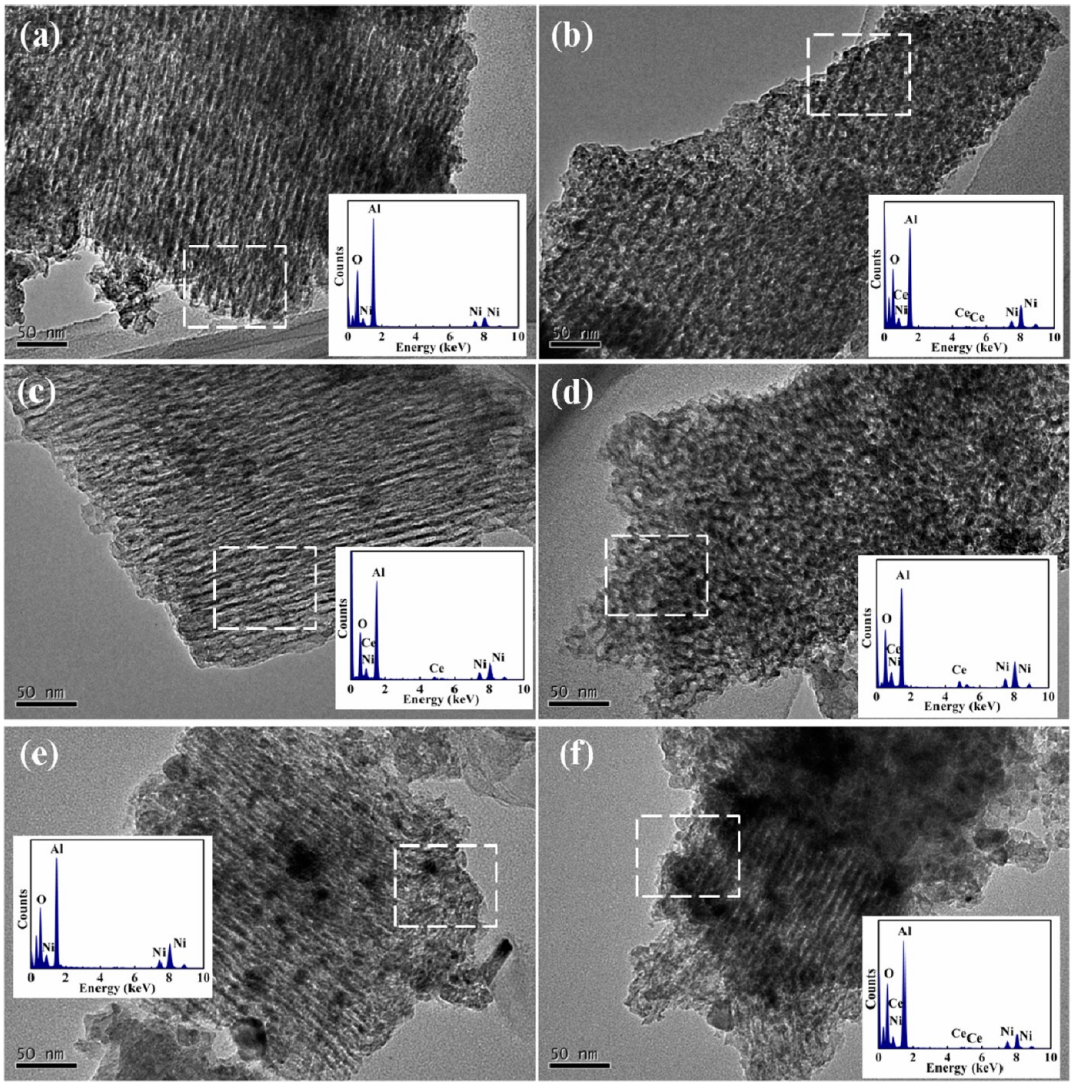

Figure 2. TEM images and the corresponding EDX spectra of various samples: (a) Ni−Al, (b) Ni−1Ce−Al, (c) Ni−2Ce−Al, (d) Ni−4Ce−Al, (e) Ni/Al-IMP, and (f) Ni/1Ce−Al-IMP.

loops shifted to higher relative pressures, characteristic for larger mesopores. Compared with that of catalysts prepared by the one-pot method, the condensation steps of the Ni-impregnated samples obviously shifted to lower P/P_0 values, indicating that with impregnation, Ni nanoparticles occupied the pores of Al_2O_3 and CeO_2−Al_2O_3 mesoporous supports and may result in the decrease of pore diameter.[35]

For the Ni−*x*Ce−Al catalysts, with an increase in the cerium content, the surface area increased to 245 m^2/g for Ni−1Ce−Al and then decreased significantly to 115 m^2/g for Ni−4Ce−Al sample. A similar trend has been observed in total pore volumes. The pore size distributions of Ni−Al and Ni−*x*Ce−Al ($x \leq 3$) were relatively narrow and centered at 3−5 nm, whereas the Ni−4Ce−Al sample showed an obviously larger pore size and a broad size distribution. Compared with the catalysts prepared by the one-pot method, an obvious reduction in surface areas, pore volumes, and average pore sizes over the Ni-impregnated catalysts was observed. This reduction was due to the blockage of pores induced by Ni species loaded into the pore channels.

Low-angle XRD patterns of the catalysts are displayed in Figure 1c. The Ni−Al sample presented a strong (100) peak around 1° together with a weak (110) peak around 1.5°, indicating that the hexagonal ordered mesoporous structure (*p6mm* symmetry) was formed in the framework of the Ni−Al materials. Similarly, an obvious (100) diffraction peak and a weak (110) peak was also detected in the Ni−*x*Ce−Al ($x \leq 3$) samples, implying that the introduction of a small amount of cerium did not destroy the mesoporous structure. The ordered mesoporous frameworks were preserved after calcination at 700 °C, showing a good thermal stability. However, it was observed that the intensity of (100) peak weakened gradually with an increase in the cerium content. The Ni−4Ce−Al sample exhibited a very weak (100) peak, suggesting that the ordered structure might collapse partially. For Ni/Al-IMP and Ni/1Ce−Al-IMP catalysts, introducing nickel species via the impregnation method decreased remarkably the intensity of the (100) peaks. This reflected that the long-range ordered mesopores were seriously blocked during the impregnation process, which could be confirmed by TEM images in Figure 2.

Wide-angle XRD patterns (Figure 1d) of Ni−Ce−Al samples showed no apparent NiO diffraction peaks, indicating that NiO nanoparticles were homogeneously dispersed in the pore channels of the samples. Via the one-pot EISA method, Ce

dx.doi.org/10.1021/cs4003113 | *ACS Catal.* 2013, 3, 1638−1651

atoms might be embedded into the mesoporous framework and segregated by Al atoms, as reported by Xu et al., resulting in a high dispersion of cerium oxide.[33]

From TEM images in Figures 2a–c, the typical ordered mesostructure was obviously observed with the regular alignment of cylindrical pores along the (110) direction. This result was in good agreement with the intense XRD peak at low angle. Moreover, it was also found that the pore channels were uniform, corresponding to the pore size listed in Table 1. In addition, the incorporation of cerium into Ni–Al oxide ($x \leq 3$) via the one-pot method did not change the ordered mesopore structure with *p6mm* hexagonal symmetry. However, with a further increase in the Ce/(Ce + Al) molar percentage up to 4%, the structure became partially disordered (Figure 2d). For Ni-impregnated catalysts, NiO particles (dark zones) were irregularly distributed on the ceria–alumina support, as observed in Figures 2e, f. Some bulk aggregates of NiO could be seen outside the mesopore channels. The Ni contents in the selected positions of Figure 2 were similar to that of the nominal values for all of the samples, as shown in Table 1.

Figure 3a, b shows the Ni $2p_{3/2}$ XPS spectra of calcined and in situ reduced catalysts, respectively. Ni 2p XPS parameters are

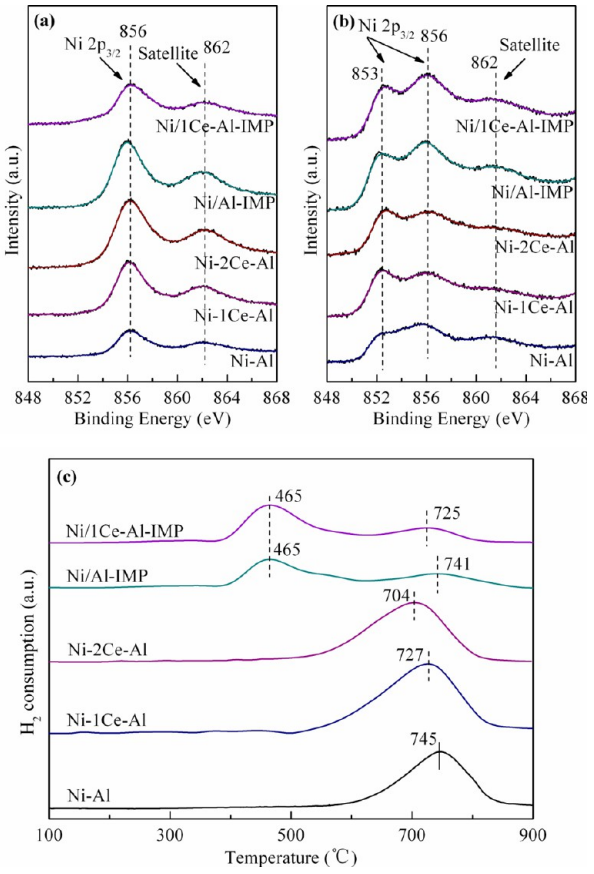

Figure 3. Ni $2p_{3/2}$ XPS spectra of (a) calcined and (b) in situ reduced catalysts. (c) TPR profiles of various catalysts.

also listed in Table 2. The calcined catalysts exhibited Ni $2p_{3/2}$ main peaks at 856.1 ± 0.1 eV with satellites around 862.0 eV and a spin–orbit coupling energy gap of 17.6 ± 0.1 eV. The reported binding energy of Ni $2p_{3/2}$ over pure NiO was about 854.4 eV.[37] This result illustrates that there is a strong metal–support interaction (SMSI) between Ni and the support.

The reduction of the catalyst was carried out in the high-pressure reaction cell attached to the preparation chamber of the XPS spectrometer. After reduction at 700 °C, new peaks of metallic Ni at 852.7 ± 0.1 eV were observed.[38] This indicated that parts of Ni^{2+} were reduced to metallic Ni while the rest of them remained as Ni^{2+}. It could be seen from Table 2 that introducing cerium with various incorporating amounts did not affect the BE of surface Ni component in catalysts. It is worth noting that more Ni^{2+} was reduced to Ni^0 over the catalysts prepared by the one-pot method compared with that over the Ni-impregnated catalysts, indicating that the catalysts prepared by the one-pot method had a higher reducibility of Ni species.

The TPR profiles of the calcined catalysts are shown in Figure 3c. Two major reduction peaks at 465 and 730 °C were observed for the Ni-impregnated catalyst. The first peak could be attributed to the reduction of bulk NiO species, which had weak interaction with the support. The second peak at 730 °C was due to the reduction of a small amount of nickel species strongly interacting with the support.[39] For the catalysts prepared by the one-pot method, there was only one reduction peak above 700 °C, which was assigned to the reduction of NiO interacting strongly with the support. This indicated that the one-step method promoted the formation of Ni species that had a strong interaction with the support.

According to refs 40 and 41, H_2 consumption peaks could be used to indicate the mobility of surface oxygen over the supports. The reduction peaks of Ni–*x*Ce–Al shifted to lower temperature, and the hydrogen consumption of Ni–*x*Ce–Al increased with increasing cerium amount. This should be attributed to the redox property of Ce ($Ce^{4+} \leftrightarrow Ce^{3+}$) and the formation of oxygen vacancies.[42] The reducibility calculated from the TPR results is summarized in Table 2. It can be seen that the one-step prepared catalysts had a higher reducibility of Ni species than that of the Ni-impregnated catalysts, which was consistent with the XPS results of the reduced samples. The percentage of Ni^0 calculated from TPR was higher than that from XPS, which was due to the different reduction conditions.

The catalysts were reduced with H_2 at 700 °C for 1 h before the XRD and TEM characterization. Figure 4 shows the XRD patterns of the reduced catalysts. In the cases of Ni/Al-IMP and Ni/1Ce–Al-IMP catalysts, the characteristic diffraction peak of γ-Al_2O_3 (JCPDS Card No. 10-0425) appeared after reduction, illustrating the phase transition from amorphous to γ-Al_2O_3 phase for the alumina skeleton. However, the mesoporous alumina framework of Ni–Al and Ni–*x*Ce–Al samples was in an amorphous state after reduction.

In addition, the diffraction peaks of Ni (JCPDS Card No. 87-0712) were also detected for all of the samples. Compared with those over Ni-impregnated samples, the diffraction peaks of Ni became wider and almost negligible for the Ni–Al and Ni–*x*Ce–Al ($x \leq 3$) samples. On the basis of the Scherrer equation, the average crystallite size of the Ni nanoparticles over Ni–Al and Ni–*x*Ce–Al ($x \leq 3$) samples was 4–5 nm. The smaller size means the higher dispersion of metal species, which could provide more active sites in methane dry reforming. However, the Ni–4Ce–Al catalyst with disordered structure had the larger crystallite size in comparison with that of Ni–*x*Ce–Al ($x \leq 3$) samples. From the results above, it was concluded that the confinement effect of the ordered mesopores resulted in the stabilization of the Ni nanoparticles.

The TEM images and nickel particle size distributions of reduced Ni–Al and Ni–*x*Ce–Al samples are shown in Figure 5. It can be found that the Ni nanoparticles are uniformly

dx.doi.org/10.1021/cs4003113 | ACS Catal. 2013, 3, 1638–1651

Table 2. The Binding Energy and Surface Composition of Ni Derived from XPS Analysis

	Ni $2p_{3/2}$ ($2p_{3/2}$–$2p_{1/2}$ gap)		composition of Ni (%)		
sample	calcined	reduced	852.6 eV (Ni^0)	856.0 eV (Ni^{2+})	degree of reduction (%)[a]
Ni–Al	856.2 (17.7)	852.6, 855.7 (17.6)	28.7	71.3	52.7
Ni–1Ce–Al	856.1 (17.6)	852.6, 856.0 (17.6)	31.7	68.3	70.7
Ni–2Ce–Al	856.2 (17.5)	852.8, 856.2 (17.5)	31.2	68.8	68.5
Ni/Al-IMP	856.0 (17.6)	852.6, 855.9 (17.7)	23.3	76.7	42.0
Ni/1Ce–Al-IMP	856.2 (17.7)	852.7, 856.0 (17.8)	24.1	75.9	47.3

[a]Degree of reduction was determined by the TPR profile.

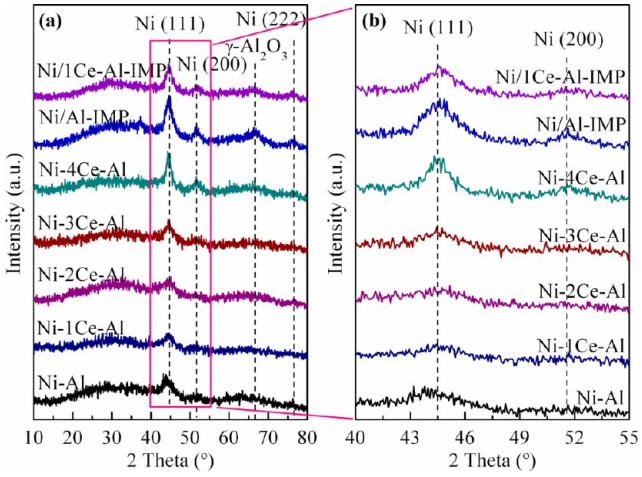

Figure 4. The XRD patterns of thereduced catalysts.

dispersed inside the pore channels of the catalysts (some dark spots, representing the nanoparticles, were placed on the framework shown in Figure 5d). The average Ni particle size for Ni–Al, Ni–1Ce–Al and Ni–2Ce–Al was 7.6, 6.0, and 6.3 nm, respectively, which was in line with the XRD and H_2-chemisorption results in Table 3. The geometrical structure is further schematically illustrated in Figure 5d to demonstrate

Table 3. The Dispersion, Particle Size, And Activation Energies (E_a) of Ni–Al and Ni–*x*Ce–Al Samples

			metal particle size[b] (nm)		
sample	metal surface area (m^2/g)	dispersion[a] (%)	D1[c]	D2[c]	E_a (kJ/mol)
Ni–Al	1.53	11.5	8.8	5.3	44.0
Ni–1Ce–Al	1.67	12.8	7.8	4.4	43.2
Ni–2Ce–Al	1.65	12.7	8.0	4.6	41.4
Ni–3Ce–Al	1.58	11.9	8.5	5.2	46.6
Ni–4Ce–Al	1.50	11.3	9.2	6.8	48.9

[a]Dispersion was calculated assuming H_{ad}/Ni_{surf} = 1. [b]Metal particle shape was assumed to be spherical. [c]D1 denotes Ni particle size of the reduced samples determined by chemisorption; D2 denotes Ni particle size of the reduced samples measured by XRD.

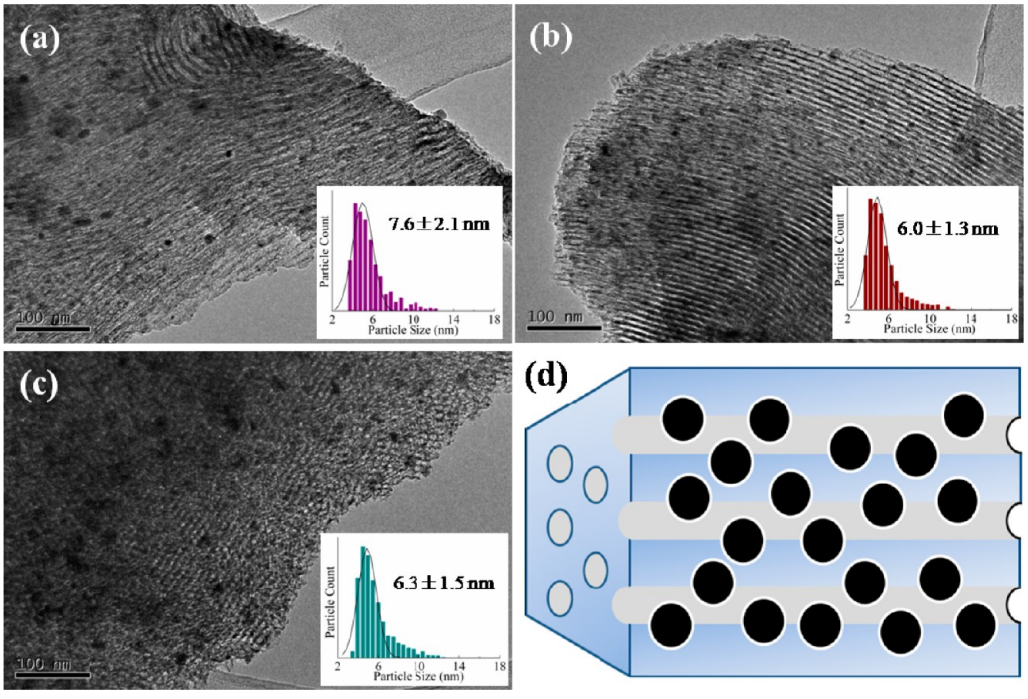

Figure 5. TEM images and nickel particle size distributions for (a) reduced Ni–Al, (b) reduced Ni–1Ce–Al, and (c) reduced Ni–2Ce–Al. (d) A schematic diagram illustrating that the Ni nanoparticles were uniformly embedded in the mesoporous alumina.

dx.doi.org/10.1021/cs4003113 | ACS Catal. 2013, 3, 1638–1651

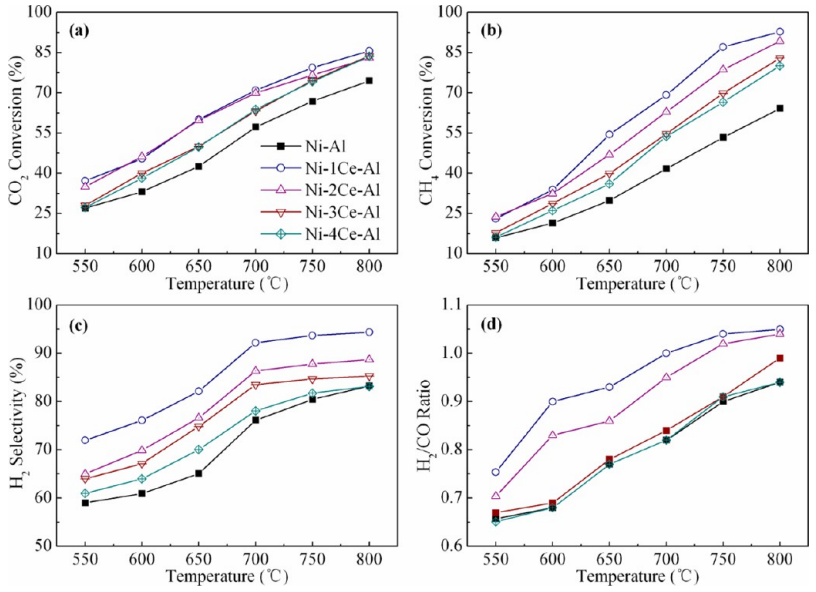

Figure 6. The effect of temperature on the initial catalytic performance of Ni−Al and Ni−*x*Ce−Al samples.

that the Ni nanoparticles were highly dispersed in the mesoporous support. For the reduced catalysts, the particle size of Ni species were a little larger than the pore size of the mesopores (as shown in Tables 1 and 3), which indicates that part of the particles should be embedded in the walls of mesopores. The phenomenon that Ni species were confined inside the mesopores resulted from the hydrophobic nature of the $Ni(acac)_2$ precursor.

3.2. Catalytic Performances of Ni−Al and Ni−Ce−Al Samples. The initial catalytic activity evaluation of Ni−Al and Ni−*x*Ce−Al samples was conducted, aiming to examine the effect of cerium incorporation on the catalytic performance. As shown in Figures 6a, b, the CO_2 and CH_4 conversions increased significantly with elevated reaction temperatures, reflecting the endothermic feature of the reforming reaction. All of the samples exhibited their highest catalytic activity at 800 °C. Higher CO_2 and CH_4 conversions were observed over Ni−*x*Ce−Al samples in comparison with those of the Ni−Al sample. Moreover, the catalytic activity was closely related to the cerium incorporation amount. When the Ce/(Ce + Al) molar percentage was 1%, the CO_2 and CH_4 conversions reached the highest values. As the cerium amount was further increased, the CO_2 and CH_4 conversions slowly decreased.

The high initial activity of Ni−1Ce−Al was attributed to the high dispersion of Ni nanoparticles and large BET surface area. In the case of Ni−1Ce−Al catalyst, Ni particles were highly dispersed in pore channels of amorphous alumina. However, with increasing the doping amount of cerium, the ordered mesostructure of Ni−*x*Ce−Al samples was partially collapsed. Hereby, some Ni particles that were not confined in the pores could grow and agglomerate during the progress of calcination and reduction to some extent. Swaan et al. reported that the initial catalytic activity was mainly relied on the nickel phase (dispersion and reduction) and little on its chemical environment (support, additive).[43] In addition, the Ni−1Ce−Al catalysts with high surface area could contact with reactants adequately. However, the surface areas of Ni−*x*Ce−Al were decreased with increasing the cerium content, resulting in the dropping activity.

At a temperature range of 550−700 °C, a higher CO_2 conversion was observed in comparison with CH_4 conversion for all of the samples. This was due to the simultaneous presence of reverse water gas-shift (RWGS) reaction ($CO_2 + H_2 \rightarrow H_2O + CO$, ΔH_{298} = +41 kJ/mol). However, as the reaction temperature increased, the CO_2 conversion was lower than the CH_4 conversion. This phenomenon may happen for two reasons: (1) as an exothermic reaction, the RWGS reaction could be inhibited with increasing reaction temperature; and (2) at a high temperature range, the thermal decomposition of methane occurred.

The H_2 selectivity increased with an increase in the reaction temperature (Figure 6c), which was due to the fact that the high temperature favored the formation of H_2 through various reactions, such as the water-gas shift reaction (WGS), carbon gasification, and methane decomposition. The cerium-incorporated samples showed obviously higher H_2 selectivity than that of Ni−Al samples. When the Ni−Al catalyst was promoted by a small amount of cerium (Ce/(Ce + Al) molar ratio = 1%), the H_2 selectivity was improved significantly. Nevertheless, with a further increase, the Ce/(Ce + Al) molar ratio, the initial H_2 selectivity decreased, showing a tendency similar to the catalytic conversion. The H_2 catalytic selectivity at 700 °C was between 76% and 86% in the cases of Ni−Al and Ni−*x*Ce−Al ($1 < x \leq 4$) samples and 92% in the case of Ni−1Ce−Al.

The H_2/CO ratios were between 0.7 and 1.15 over the whole range of temperatures studied and were elevated with increasing temperature (Figure 6d). These ratios were observed to be less than unity at low temperatures, which was due to the fact that the side reactions, such as RWGS and methanation reaction, could consume H_2 at low temperatures.[23] However, these values were more than unity at high temperatures. This could be due to the fact that high temperature facilitated the production of H_2 through water-gas shift reaction (WGS), carbon gasification, and methane decomposition.[23]

The turnover frequency (TOF) of the reaction over Ni−Al and Ni−*x*Ce−Al catalysts was calculated by normalizing the observed reaction rate (mol $CH_4/(s \cdot g_{cat})$) to the number of exposed Ni atoms per gram of catalyst (mol Ni/g_{cat}). Because the dissociative adsorption of methane was considered to be the

dx.doi.org/10.1021/cs4003113 | ACS Catal. 2013, 3, 1638−1651

rate-determining step, the reaction rate was calculated using the methane conversion.[44] As displayed in Figure 7a, the TOF

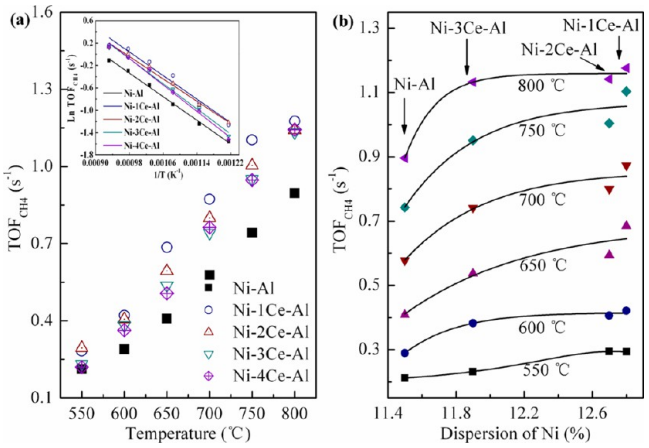

Figure 7. (a) Comparison of TOFs of CH_4 conversion over Ni−Al and Ni−*x*Ce−Al catalysts. The inset shows the corresponding Arrhenius plots. (b) TOF_{CH_4} versus Ni dispersion over Ni−Al and Ni−*x*Ce−Al catalysts.

values of Ni−*x*Ce−Al samples were higher than that of the Ni−Al sample. The difference in TOF values between the different catalysts can be from the changes in dispersion or particle size of Ni active species.[45] In this study, the TOF values changed significantly when the level of Ni dispersion was changed. A relationship between active metal dispersion and TOF in methane dry reforming has been reported by other investigators.[46,47] For example, the impact of the Rh particle size on the TOF was investigated by Zhang et al.[46] It was found that the TOF values decreased with an increase in the Rh particle size over Al_2O_3 and TiO_2 supported catalysts. Wang et al. also observed that the methane dry reforming was sensitive to the Ni dispersion, and the TOF increased with a reduction in the Ni particle size over Ni/MgO catalysts.[47]

It should be mentioned that the Ni−*x*Ce−Al catalysts exhibited comparable or enhanced TOF values as compared with those reported in the previous literature.[22,47,48] Liu et al. reported higher TOF_{CH_4} values (0.82−1.2 s^{-1}) over Ni−Zr/MCM-41 catalysts as compared with Ni/MCM-41 (0.75 s^{-1}) at 750 °C.[22] This was attributed to the ability of the Zr^{4+} species to activate CO_2 and the formation of highly dispersed Ni particles as a result of the anchoring effect of Zr^{4+} species. Similar TOF results were also reported for noble metal catalysts.[48] Using α-Al_2O_3- and ZrO_2-supported Pt catalysts, a high activity with TOF_{CH_4} values between 1 and 1.7 s^{-1} were reported, and the Ni-based catalysts presented a higher activity, with TOF_{CH_4} values of 1.7−3.7 s^{-1}.[48] For Ni/MgO catalysts, high TOF_{CH_4} values were observed in the range of 1.5−3.8 s^{-1} under the GHSVs between 16 000 and 48 000 mL/(h·g_{cat}), which was ascribed to the strong interaction of Ni nanoparticles with the $Ni_xMg_{1-x}O$ solid solution support.[47]

From the Arrhenius plots in Figure 7a, on the basis of methane conversion data, we obtained the related apparent activation energies (E_a). In the literature, the E_a's for Ni-based catalysts applied in methane dry reforming were reported to vary considerably (29.3−360 kJ/mol), depending on the nature of the support, the addition of promoters, the catalytic tests conditions (i.e., space velocity), etc.[49,50] Our results were of the same order of magnitude. In our study, it was also evident that cerium modifier had a great influence on the E_a value of the mesoporous Ni−Al catalyst. As shown in Table 3, the E_a value of Ni−1Ce−Al and Ni−2Ce−Al samples was estimated to be 43.2 and 41.4 kJ/mol, respectively, in contrast to the higher value of 44.0 kJ/mol for the Ni−Al catalyst. This clearly indicated the considerably higher catalytic activity of the Ni−*x*Ce−Al ($x \leq 2$) than that of the reference sample. However, with the Ce/(Ce + Al) percentage ratio further increasing upon 4%, the activation barrier became higher and the E_a value sharply increased. The activation energies were comparable with those available in the literature.[44,46]

The "low-temperature step" was not observed in Arrhenius plots. This step could be clearly seen with MCM-41-supported catalysts for methane combustion, which was related to the presence of internal diffusion in the long cylindrical channels of

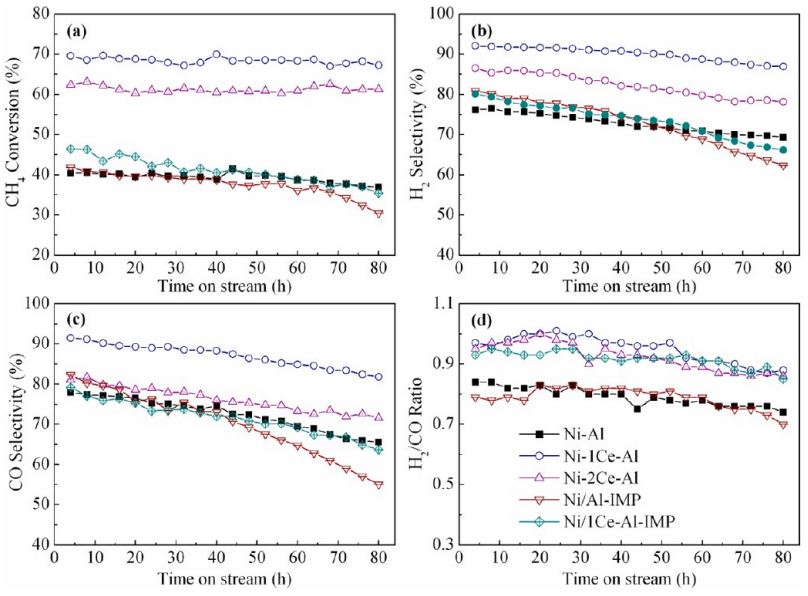

Figure 8. Catalytic stability test of the representative samples for methane dry reforming at 700 °C for 80 h.

dx.doi.org/10.1021/cs4003113 | ACS Catal. 2013, 3, 1638−1651

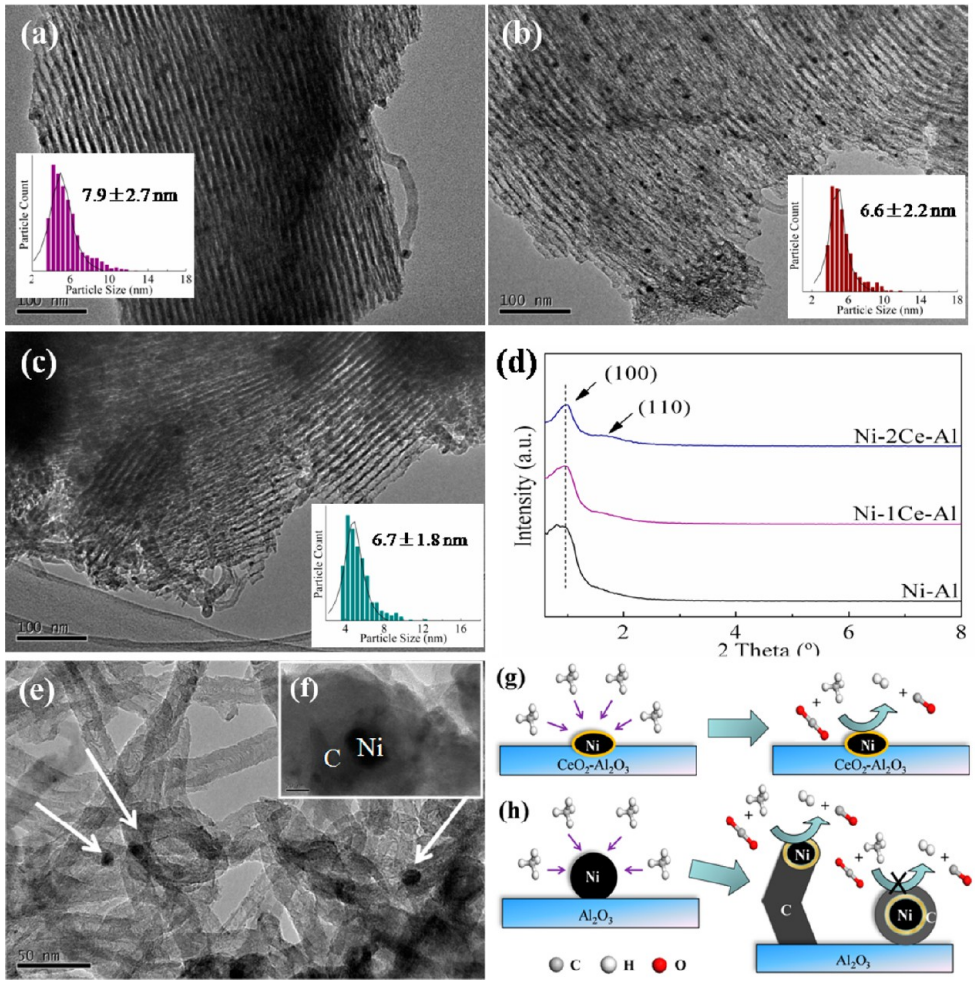

Figure 9. TEM images for (a) spent Ni−Al, (b) spent Ni−1Ce−Al, and (c) spent Ni−2Ce−Al, respectively. (d) Low-angle XRD patterns of spent Ni−Al, Ni−1Ce−Al, and Ni−2Ce−Al catalysts. TEM micrographs of carbon species on spent Ni/Al-IMP: (e) filamentous carbon and (f) encapsulating carbon. Schematic representation of methane dry reforming over (g) Ni−1Ce−Al and (h) Ni/Al-IMP samples.

the MCM-41 support.[51] However, there was much less diffusion limitation in the present Ni−Al and Ni−*x*Ce−Al catalysts because of the large pore size of these materials. This step also could not be found with SBA-15-supported catalysts.[52]

To elucidate the effect of Ni dispersion on the TOF values, we studied the change in the TOF_{CH_4} with the variation of Ni dispersion on the Ni−Al and Ni−*x*Ce−Al catalysts. As shown in Figure 7b, the TOF values of CH_4 increased with increasing Ni dispersion. Thus, the catalytic activity expressed by the TOF of CH_4 was of the function TOF = *f* (Ni dispersion) for the Ni−Al and Ni−*x*Ce−Al catalysts. This reflected that the TOF at the beginning of the reaction was related to the Ni dispersion.

To investigate the catalytic stability of the various Ni catalysts, a constant temperature test was carried out at 700 °C for 80 h, and the results are shown in Figure 8. The Ni−*x*Ce−Al samples exhibited higher catalytic activity and long-term stability than Ni−Al and Ni-impregnated catalysts. The CH_4 conversions remained stable, and no deactivation was observed throughout 80 h of time on-stream (TOS) for Ni−*x*Ce−Al samples. This excellent behavior was closely associated with the confinement effect of the mesostructure for stabilization of the Ni active species as well as the incorporation of the cerium promoter. Ni-impregnated samples exhibited relatively poor activity and stability, with Ni/Al-IMP being poorer than Ni/1Ce−Al-IMP. After 80 h of TOS, the sequence of CH_4 conversion was as follows: Ni−1Ce−Al (66.2%) > Ni−2Ce−Al (60.3%) > Ni−Al (35.9%) > Ni/Ce−Al-IMP (34.4%) > Ni/Al-IMP (29.4%). Combining the XRD analysis and catalytic stability results, it could be seen that the Ni particle size was a key factor that affected the behavior of the catalyst, and the formation of Ni particles of smaller size was beneficial for methane dry reforming.

The ordered mesoporous catalysts incorporated with various metals have been studied in methane dry reforming.[53,54] In our previous work, the catalytic properties of Ce−SBA-15-supported Ni catalysts were tested.[53] During 40 h of stability evaluation, the CH_4 conversion decreased from 74% to 71%. Under the conditions of CO_2/CH_4 = 1 and GHSV = 15 000 mL/(h·g_{cat}), the mesoporous MgO−Al_2O_3-supported Ni catalysts exhibited rather stable catalytic performance during 100 h of TOS, which was ascribed to the more exposed active sites in the mesoporous framework of the supports.[54]

The H_2 and CO selectivity, together with the H_2/CO ratio, were tested during the stability. As displayed in Figure 8b−d, the Ni−*x*Ce−Al sample maintained high H_2 and CO selectivity and H_2/CO ratio during 80 h of TOS, but the Ni−Al sample showed moderate initial H_2 and CO selectivity, which deactivated gradually with TOS. The Ni-impregnated samples presented analogous moderate initial H_2 and CO selectivity

dx.doi.org/10.1021/cs4003113 | *ACS Catal.* 2013, 3, 1638−1651

with the Ni−2Ce−Al sample. As the reaction proceeded, a decrease in selectivity was observed for Ni-impregnated samples. The poor catalytic behavior and unexpected product selectivity for the Ni-impregnated samples reflected the lack of accessible active centers for methane dry reforming. The H_2/CO ratios for all of the samples were lower than unity, reflecting a great tendency toward the formation of H_2O through RWGS reaction.[55] The detection of H_2O in the outlet also indicated the occurrence of this reaction. The lower H_2/CO ratios over Ni−Al and Ni/Al-IMP catalysts indicated that the RWGS easily occurred over catalysts without cerium incorporation because of the presence of more unreacted CO_2. This phenomenon was also reported in previous literature.[21,56]

3.3. Deactivation Analysis. In this study, the spent samples after 80 h of TOS at 700 °C were characterized by XRD, TGA, TPH, and TEM to investigate the factors resulting in the deactivation of Ni−Al and Ni-impregnated catalysts.

Figure 9 showed the TEM images as well as low-angle XRD patterns of spent Ni−*x*Ce−Al catalysts after 80 h of TOS. From Figure 9a−c, it could be observed that the well-dispersed Ni nanoparticles and highly ordered mesostructure still remained after the stability test, and no large particles were found over the samples. The average Ni particle size was 7.9, 6.6, and 6.7 nm for spent Ni−Al, Ni−1Ce−Al, and Ni−2Ce−Al catalysts, respectively. From the low-angle patterns, a main diffraction peak accompanied by a minor peak attributed to (100) and (110) plane reflection could be seen, which were characteristic of the mesoporous order of Ni−*x*Ce−Al catalysts after the stability test.

From wide-angle XRD patterns in Figure 10, the γ-Al_2O_3 diffraction peak appeared for the spent Ni−Al sample,

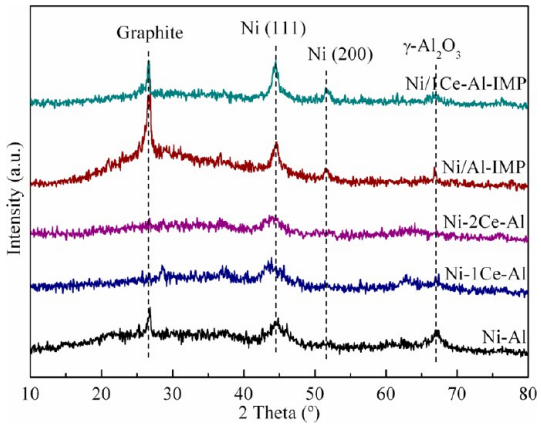

Figure 10. XRD patterns of spent Ni-supported samples.

indicating a phase transition to the γ-Al_2O_3 crystalline phase from the amorphous phase took place during the long-term stability test. However, the mesoporous framework of alumina in Ni−*x*Ce−Al samples was almost still in an amorphous state. The diffraction peaks belonging to the metallic nickel phase were detected after reaction for all samples, and the diffraction intensities of metallic nickel for Ni−Al and Ni−*x*Ce−Al catalysts were still weak after the stability test. It demonstrated that the sintering of Ni nanoparticles was avoided to some extent as a result of the confinement effect of the alumina mesoporous framework. The average Ni crystallite sizes increased in the following sequence: Ni/1Ce−Al-IMP (8.1 nm) ≈ Ni/Al-IMP (7.9 nm) < Ni−Al (5.6 nm) < Ni−1Ce−Al (5.0 nm) ≈ Ni−2Ce−Al (4.8 nm). The presence of a large nickel particle size for Ni-impregnated catalysts indicated the occurrence of Ni particle sintering during the stability test. Some Ni particles were located on the external surface of the alumina framework, which could not be confined by the pore channels of mesoporous material. The thermal agglomeration of the Ni particles took place under harsh conditions during the reforming reaction.

Obvious diffraction peaks of graphitic carbon were found at a 2θ value of 26° over Ni−Al and Ni-impregnated samples. The intensity of the graphite peak increased in the following sequence: Ni/1Ce−Al-IMP < Ni−Al < Ni/Al-IMP. This indicates that large amounts of coke deposited on the surface of the spent Ni−Al and Ni-impregnated samples. Compared with Ni−Al and Ni/1Ce−Al-IMP catalysts, the Ni/Al-IMP sample exhibited a higher intensity of the graphite peak. This suggests that more carbon species were formed on the Ni/Al-IMP catalyst. However, in the cases of spent Ni−*x*Ce−Al samples, no diffraction peaks of graphitic carbon were found, which was due to the excellent resistance to coke formation.

The high dispersion of Ni nanoparticles could inhibit carbon deposition and was favorable to the high activity. Because of the larger particle size of the Ni species over Ni-impregnated catalysts as compared with that over samples prepared by the one-pot method, the rate of accumulation of carbon species and further transformation into less-active carbon were favored.

In the cases of the one-pot-prepared samples, the Ni particles were anchored by the alumina matrix, resulting in a strong metal−support interaction between Ni and the alumina framework (Figure 3c and Figure 9g). Thus, it was difficult for the carbon to lift the Ni particle from the support. However, in the case of the Ni/Al-IMP catalyst, because of the weak interaction between Ni and the support, the movement of Ni particles within the internal channels or from internal mesopores to the external surface of the mesoporous alumina could occur under harsh reaction conditions. The carbon species could dissolve in the Ni particles and diffuse through it to detach the Ni particles from the support (Figure 9e, h). These Ni particles were probably agglomerated during the reaction. Therefore, some Ni particles with a size of 15−20 nm were observed in the TEM images in Figure 9e and f. However, the nickel particle sizes over the reduced and spent Ni−*x*Ce−Al samples were no more than 10 nm.

The TG/DTA profiles of spent catalysts are shown in Figure 11. TG curves were used to quantify the weight loss derived

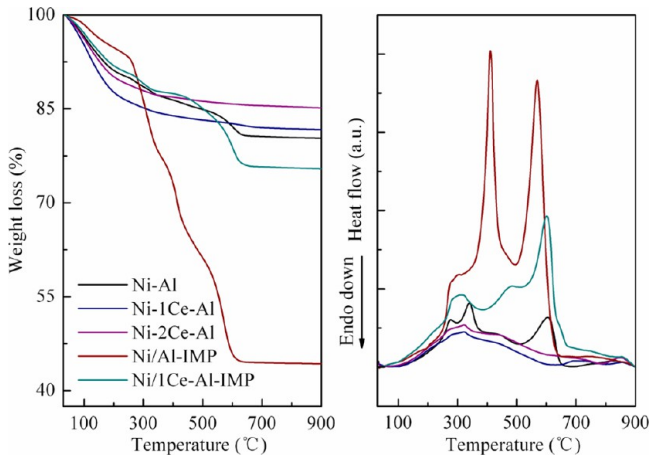

Figure 11. TG/DTA profiles of spent samples.

dx.doi.org/10.1021/cs4003113 | ACS Catal. 2013, 3, 1638−1651

from the removal of carbon. The weight loss over the Ni-impregnated samples was obviously larger than that over catalysts prepared by the one-pot method. The total weight loss of spent samples increased in the following sequence: Ni−2Ce−Al (14.9%) < Ni−1Ce−Al (18.4%) < Ni−Al (19.7%) < Ni/1Ce−Al-IMP (24.6%) < Ni/Al-IMP (55.8%). This observation illustrates that carbon deposition on the catalyst surface was greatly inhibited for the catalysts prepared by one-pot procedure.

In the case of the Ni−Al sample, two exothermic peaks were observed in DTA profiles, implying that there were two types of carbon species deposited on Ni active sites. The first peak between 250 and 350 °C was ascribed to the combustion of amorphous carbon (α-carbon), which was the active species for the formation of syngas.[57] The peak above 550 °C was attributed to the oxidation of inert carbon with different degrees of graphitization (γ-carbon), which was responsible for the deactivation of the catalyst.[21,58] There was only one exothermic peak around 300 °C for the Ni−xCe−Al samples, indicating that the carbon species formed over Ni−xCe−Al catalysts were mainly relatively active carbon species. The active carbons were preferentially formed during the early stage of reforming, mainly through methane decomposition. Part of the active carbon species could be transformed to less-active carbon species (β-carbon) through further dehydrogenation, polymerization, and rearrangement. The peak between 350 and 500 °C over Ni-impregnated samples could correspond to β-carbon.[43,58] Moreover, large amounts of graphitic carbon species (γ-carbon) were observed over spent Ni-impregnated sample. It was in line with the XRD patterns of spent samples, which showed a high intensity for the graphite peak. When only inert carbon was considered, the deposited carbon amount increased in the following sequence: Ni−2Ce−Al (1.3%) ≈ Ni−1Ce−Al (1.4%) < Ni−Al (4.6%) < Ni/1Ce−Al-IMP (9.5%) < Ni/Al-IMP (16.7%).

The TPH profiles of spent catalysts are shown in Figure 12. The hydrogenation temperature implied the activity of surface

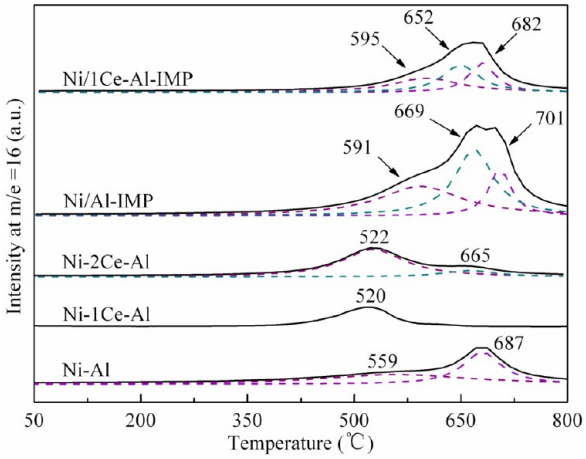

Figure 12. TPH profiles of spent catalysts.

carbon, and the lower hydrogenation temperature showed the higher activity of the surface carbon. Over the Ni−xCe−Al samples, α-carbon between 500 and 600 °C was clearly observed, and negligible β-carbon was found. Ni-impregnated catalysts were found to exhibit a higher intensity of graphite compared with the one-pot prepared catalyst. The tendency to form carbon deposits over the spent samples was in good agreement with the TG analysis. The presence of difficultly removed γ-carbon was associated with the deactivation of Ni−Al and Ni-impregnated catalysts.

It is worth noting that the carbon deposition was significantly suppressed over cerium-modified catalysts in comparison with the catalysts without cerium modification. This was due to the fact that the oxygen mobility of CeO_2 promoted the activation and reduction of CO_2. During the reforming reaction, Ce_2O_3 formed from the reduction of CeO_2 under H_2 atmosphere was reoxidized by CO_2. The obtained CeO_2 could eliminate carbon deposition that was formed on the active Ni surface by methane cracking. The rate of coke gasification and the rate of coking deposition nearly achieved equality, which resulted in the stable catalytic performance. The redox cycling property of Ce^{3+}/Ce^{4+} promoted the gasification of deposited carbon. This process is expressed in Scheme 2 and summarized by following reactions:

$$2CeO_2 + H_2 \rightarrow Ce_2O_3 + H_2O \quad (1)$$

$$CH_4 + Ni \rightarrow Ni{-}C + 2H_2 \quad (2)$$

$$Ce_2O_3 + CO_2 \rightarrow 2CeO_2 + CO \quad (3)$$

$$2CeO_2 + Ni{-}C \rightarrow Ce_2O_3 + Ni + CO \quad (4)$$

Scheme 2. Mechanism of Methane Dry Reforming over Ni−Ce−Al Mesoporous Catalysts

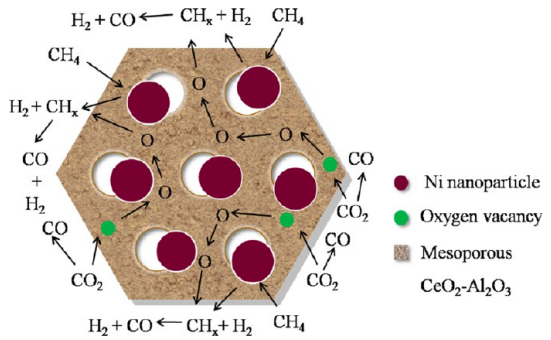

To provide supports to prove this reaction mechanism, the Ce 3d XPS spectra of the Ni−1Ce−Al catalyst before and after reduction, O 1s XPS spectra of reduced Ni−Al and Ni−1Ce−Al, and with the C 1s XPS spectra of spent Ni−1Ce−Al catalyst are given.

The spectra of Ce 3d for calcined and reduced Ni−1Ce−Al catalyst are analyzed in Figure 13a. The two groups of spin−orbital multiplets, corresponding to $3d_{3/2}$ and $3d_{5/2}$, are denoted as u and v, respectively. For the calcined sample, there are three main $3d_{5/2}$ peaks at about 883.4 (v), 889.3 (v_2), and 898.6 (v_3) eV and three main $3d_{3/2}$ peaks at about 901.7 (u), 907.5 (u_2), and 916.7 (u_3) eV, all of which are attributed to the Ce^{4+} state. The peaks near 886.3 eV (v_1) and 904.1 eV (u_1) could be attributed to the Ce^{3+} state. Therefore, the valence of cerium over the surface of calcined Ni−1Ce−Al catalyst is mainly in a 4+ oxidation state with a small amount of Ce^{3+}. The Ce^{3+} content can be estimated from the area of u_1 and v_1 according the following equation:

$$Ce^{3+}\,(\%) = \frac{S_{u1} + S_{v1}}{\sum (S_u + S_v)} \times 100$$

The relative contents of Ce^{3+} calculated for calcined and reduced Ni−1Ce−Al catalysts are given in Table 4. It can be

dx.doi.org/10.1021/cs4003113 | ACS Catal. 2013, 3, 1638−1651

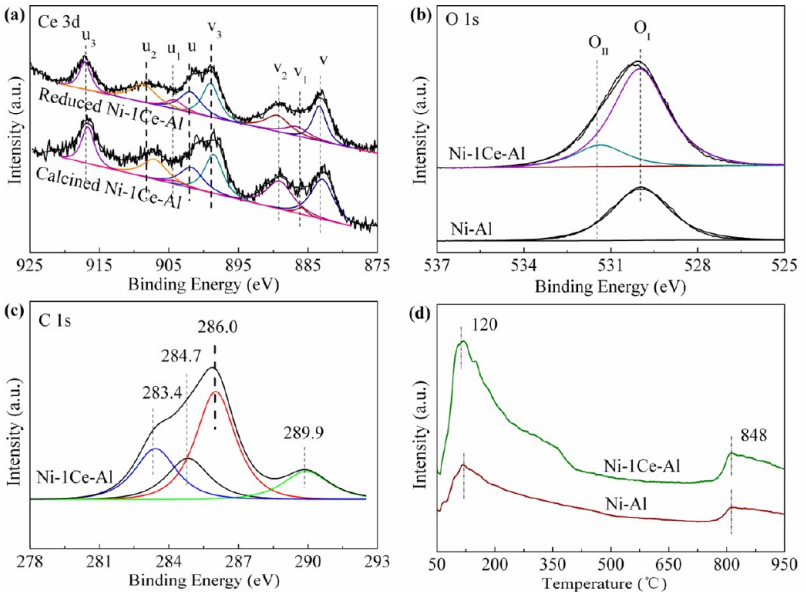

Figure 13. (a) Ce 3d XPS spectra of the Ni−1Ce−Al catalyst before and after reduction, (b) O 1s XPS spectra of reduced Ni−Al and Ni−1Ce−Al catalysts, (c) C 1s XPS spectra of the spent Ni−1Ce−Al catalyst, and (d) O_2-TPD profiles of Ni−Al and Ni−1Ce−Al catalysts.

Table 4. Surface XPS Compositions of Ni−Al and Ni−1Ce−Al Catalysts

	atomic ratio by XPS	
sample	$Ce^{3+}/(Ce^{3+} + Ce^{4+})$ (%)	$O_{II}/(O_I + O_{II})$ (%)
reduced Ni−Al		0.0
fresh Ni−1Ce−Al	2.9	
reduced Ni−1Ce−Al	18.5	16.9

found that the percentage of Ce^{3+} in the reduced sample was much higher than that in the calcined sample, indicating that Ce^{4+} was reduced to Ce^{3+} during the H_2 thermal treatment (reaction 1).

The spectra of O 1s for reduced Ni−Al and Ni−1Ce−Al samples were fitted with two Gassian peaks, as shown in Figure 13b. The oxygen mobility was closely related to oxygen vacancies, and oxygen vacancies can be detected through the O 1s XPS.[5] The samples were pretreated with CO_2 at 700 °C before scanning, so there was no XPS signal of adsorbed water.[5] There were two oxygen species. The low binding energy peak was attributed to the surface lattice oxygen, and the high binding energy one, to the chemisorbed oxygen (adsorbed −OH in water and C−O in CO_3^{2-}). Palmqvist et al.[59] reported that the XPS peaks of the adsorbed oxygen were derived from carbonate species trapped by oxygen vacancies, so the amount of oxygen vacancies can be obtained from the XPS relative percentage of adsorbed oxygen. The XPS results of the lattice oxygen (O_I) and the adsorbed oxygen (O_{II}) are shown in Table 4. The peak area of adsorbed oxygen (or O_{II}/O_I ratio) increased obviously for Ni−1Ce−Al compared with that for Ni−Al, which was almost negligible, suggesting an increase in oxygen vacancies. The oxygen vacancies acted as the active site for activating CO_2, and the activated CO_2 could react with the deposited carbon (reaction 3).[60,61]

The O_2-TPD profiles are shown in Figure 13d. Two desorption peaks of oxygen were observed in both catalysts, the peak temperatures of which were at 120 and 848 °C. The first desorption peak was ascribed to the desorption of surface adsorbed oxygen species, and the second one corresponded to the desorption of lattice oxygen.[5] From the O 1s XPS and O_2-TPD results, it can be seen that there were a higher content of surface oxygen species and an easier migration of bulk lattice oxygen species to the surface in Ni−1Ce−Al sample, as compared with that over the Ni−Al sample. This not only promoted the reaction 4 but also favored the replenishment of the consumed oxygen species. Because of more either surface lattice oxygen species or bulk lattice oxygen species in Ni−1Ce−Al than that in Ni−Al, Ni−1Ce−Al possessed a higher activity than Ni−Al.

The formation of Ni−C during the reaction could be proved by the C 1s XPS spectra of the spent Ni−1Ce−Al catalyst, as displayed in Figure 13c. There were four types of surface carbon species for the spent Ni−1Ce−Al sample. The C1s binding energies at 289.9, 286.0, 284.8, and 283.4 eV were attributed to surface oxidized carbon species, CH_4 cracking fragments CH_x (x = 0∼3), nonactivated carbon, and metallic carbide (Ni−C), respectively. Baker et al.[62] and An et al.[63] have reported that metallic carbide (Ni−C) formed by methane dissociation on metal surfaces was an activated intermediate species that was easily gasified by CO_2 (reaction 2 and 4).

Daza et al. studied CeO_2-doped Ni−Mg−Al periclase oxide catalysts obtained from hydrotalcites for methane dry reforming.[64] They also confirmed the positive effect of cerium incorporation for the inhibition of carbon deposition. Similarly, a study by Yang et al. demonstrated that the carbon deposition on Ni/γ-Al_2O_3 catalyst promoted with CeO_2 was significantly inhibited in the reforming reaction, resulting in better long-term stability.[65] In our previous work, modification of SBA-15 with CeO_2 over Ni catalyst was also found to be promising.[53]

By incorporating cerium into the alumina framework, a clear improvement in the Ni dispersion, long-term stability, and a low deactivation rate was seen (see Figures 4, 8, 11). Similar to the anchoring effect reported by Liu et al.,[22] the enhanced catalytic stability could be associated with the confinement of highly dispersed Ni clusters by the alumina framework. In summary, the higher catalytic stability over Ni−Ce−Al could be attributed to the confinement effect of alumina as well as the oxygen mobility properties of cerium.

dx.doi.org/10.1021/cs4003113 | ACS Catal. 2013, 3, 1638−1651

4. CONCLUSIONS

Ordered mesoporous Ni−Al and Ni−Ce−Al materials with various cerium contents were prepared using an improved one-pot EISA method and were used as catalysts for methane dry reforming reaction. Via this simple route, a hydrophobic nickel precursor could be directly incorporated into the hydrophobic cores of surfactant micelles P123, and thus, well-dispersed Ni nanoparticles could be stabilized by the confinement effect of the mesoporous alumina matrix. Characterization results revealed that the mesoporous Ni−1Ce−Al and Ni−2Ce−Al samples possessed a superior thermal stability and larger specific surface areas and pore volumes compared with the Ni−Al catalyst. In comparison with that of Ni-impregnated catalyst, the Ni−Al and cerium-incorporated Ni−Al catalysts prepared by the one-pot method presented enhanced long-term stability. The improved catalytic stability was closely associated with both stabilizations of the active nickel particles by alumina framework and higher oxygen mobility of cerium-incorporated samples. The ordered mesoporous structure for Ni−Al and Ni−Ce−Al samples was retained after reaction at 700 °C for 80 h, and the Ni−Ce−Al catalysts showed excellent resistance to formations of graphitic carbon species. The XRD and TGA results showed that large amounts of graphitic carbon species were formed over Ni-impregnated catalysts, which was responsible for the loss of activity.

AUTHOR INFORMATION

Corresponding Author

*E-mail: (W.Q.) qianwz@tsinghua.edu.cn, (W.C.) chuwei65@yahoo.com.cn.

Notes

The authors declare no competing financial interest.

ACKNOWLEDGMENTS

This work was supported by Natural Science Foundation of China (key program, 51236004), the Fundamental Research Funds for the Central Universities of China (2010SCU22010), the Special Funds for Scientific Research on Public Causes of China (201010236) and the National Basic Research Program of China (973 Program, No. 2011CB201202). The authors thank Zhenxin Xu, Yanyan Feng, and Xiangfeng Hu for their helpful discussions.

REFERENCES

(1) Ha, K. S.; Bae, J. W.; Woo, K. J.; Jun, K. W. *Environ. Sci. Technol.* **2010**, *44*, 1412.
(2) Hunt, A. J.; Sin, E. H. K.; Marriott, R.; Clark, J. H. *ChemSusChem* **2010**, *3*, 306.
(3) Fan, M. S.; Abdullah, A. Z.; Bhatia, S. *ChemSusChem* **2011**, *4*, 1643.
(4) Chu, W.; Ran, M.; Zhang, X.; Wang, N.; Wang, Y.; Xie, H.; Zhao, X. S. *J. Energy Chem.* **2013**, *22*, 136.
(5) Wang, N.; Chu, W.; Zhang, T.; Zhao, X. S. *Chem. Eng. J.* **2011**, *70*, 457.
(6) Gonzalez-Delacruz, V. M.; Pereñiguez, R.; Ternero, F.; Holgado, J. P.; Caballero, A. *ACS Catal.* **2011**, *1*, 82.
(7) Yu, X. P.; Wang, N.; Chu, W.; Liu, M. *Chem. Eng. J.* **2012**, *209*, 623.
(8) Chu, W.; Wang, L. N.; Chernavskii, P. A.; Khodakov, A. Y. *Angew. Chem., Int. Ed.* **2008**, *47*, 5052.
(9) Wei, J. M.; Xu, B. Q.; Li, J. L.; Cheng, Z. X.; Zhu, Q. M. *Appl. Catal., A* **2000**, *196*, L167−L172.
(10) Gronchi, P.; Centola, P.; Rosso, R. D. *Appl. Catal., A* **1997**, *24*, 83.
(11) Chen, J.; Yao, C.; Zhao, Y.; Jia, P. *Int. J. Hydrogen Energy* **2010**, *35*, 1630.
(12) García-Diéguez, M.; Pieta, I. S.; Herrera, M. C.; Larrubia, M. A.; Malpartida, I.; Alemany, L. J. *Catal. Today* **2010**, *149*, 380.
(13) Damyanova, S.; Pawelec, B.; Arishtirova, K.; Fierro, J. L. G.; Sener, C.; Dogu, T. *Appl. Catal., B* **2009**, *92*, 250.
(14) Zhao, Y.; Pan, Y.; Xie, Y.; Liu, C. *Catal. Commun.* **2008**, *9*, 1558.
(15) Tomishige, K.; Chen, Y.; Fujimoto, K. *J. Catal.* **1999**, *181*, 91.
(16) Wang, J. B.; Wu, Y. S.; Huang, T. J. *Appl. Catal., A* **2004**, *272*, 289.
(17) Hou, Z.; Gao, J.; Guo, J.; Liang, D.; Lou, H.; Zheng, X. *J. Catal.* **2007**, *250*, 331.
(18) Zhang, J.; Wang, H.; Dalai, A. K. *Appl. Catal., A* **2008**, *339*, 121.
(19) Sun, N.; Wen, X.; Wang, F.; Wei, W.; Sun, Y. *Energy Environ. Sci.* **2010**, *3*, 366.
(20) van Dillen, A. J.; Terörde, R. J. A. M.; Lensveld, D. J.; Geus, J. W.; de Jong, K. P. *J. Catal.* **2003**, *216*, 257.
(21) Liu, D.; Quek, X. Y.; Adeline Wah, H. H.; Zeng, G.; Li, Y.; Yang, Y. *Catal. Today* **2009**, *148*, 243.
(22) Liu, D.; Quek, X. Y.; Cheo, W. N. E.; Lau, R.; Borgna, A.; Yang, Y. *J. Catal.* **2009**, *266*, 380.
(23) Quek, X. Y.; Liu, D.; Cheo, W. N. E.; Wang, H.; Chen, Y.; Yang, Y. *Appl. Catal., B* **2010**, *95*, 374.
(24) Sun, J.; Ma, D.; Zhang, H.; Liu, X.; Han, X.; Bao, X.; Weinberg, G.; Pfänder, N.; Su, D. *J. Am. Chem. Soc.* **2006**, *128*, 15756.
(25) Liu, S.; Guan, L.; Li, J.; Zhao, N.; Wei, W.; Sun, Y. *Fuel* **2008**, *87*, 2477.
(26) Sokolov, S.; Kondratenko, E. V.; Pohl, M. M.; Barkschat, A.; Rodemerck, U. *Appl. Catal., B* **2012**, *113−114*, 19.
(27) Xu, L.; Song, H.; Chou, L. *Int. J. Hydrogen Energy* **2012**, *37*, 18001.
(28) Wu, Z.; Li, Q.; Feng, D.; Webley, P. A.; Zhao, D. *J. Am. Chem. Soc.* **2010**, *132*, 12042.
(29) Yuan, Q.; Yin, A. X.; Luo, C.; Sun, L. D.; Zhang, Y. W.; Duan, W. T.; Liu, H. C.; Yan, C. H. *J. Am. Chem. Soc.* **2008**, *130*, 3465.
(30) Cai, W.; Yu, J.; Anand, C.; Vinu, A.; Jaroniec, M. *Chem. Mater.* **2011**, *23*, 1147.
(31) Yuan, Q.; Liu, Q.; Song, W. G.; Feng, W.; Pu, W. L.; Sun, L. D.; Zhang, Y. W.; Yan, C. H. *J. Am. Chem. Soc.* **2007**, *129*, 6698.
(32) Horiguchi, J.; Kobayashi, Y.; Kobayashi, S.; Yamazaki, Y.; Omata, K.; Nagao, D.; Konno, M.; Yamada, M. *Appl. Catal., A* **2011**, *392*, 86.
(33) Xu, L.; Song, H.; Chou, L. *ACS Catal.* **2012**, *2*, 1331.
(34) Andreeva, D.; Ivanov, I.; Ilieva, L.; Abrashev, M. V. *Appl. Catal., A* **2006**, *302*, 127.
(35) Morris, S. M.; Fulvio, P. F.; Jaroniec, M. *J. Am. Chem. Soc.* **2008**, *130*, 15210.
(36) Shen, W.; Komatsubara, K.; Hagiyama, T.; Yoshida, A.; Naito, S. *Chem. Commun.* **2009**, *42*, 6490.
(37) Lemonidou, A. A.; Goula, M. A.; Vasalos, I. A. *Catal. Today* **1998**, *46*, 175.
(38) Özkara-Aydınoğlu, Ş.; Aksoylu, A. E. *Int. J. Hydrogen Energy* **2011**, *36*, 2950.
(39) Wang, K.; Li, X.; Ji, S.; Shi, X.; Tang, J. *Energy Fuels* **2009**, *23*, 25.
(40) Sun, G. B.; Hidajat, K.; Wu, X. S.; Kawi, S. *Appl. Catal., B* **2008**, *81*, 303.
(41) Lin, S. S.; Chen, C. L.; Chang, D. J.; Chen, C. C. *Water Res.* **2002**, *36*, 3009.
(42) Campbell, C. T.; Peden, C. H. F. *Science* **2005**, *309*, 713.
(43) Swaan, H. M.; Kroll, V. C. H.; Martin, G. A.; Mirodatos, C. *Catal. Today* **1994**, *21*, 571.
(44) Kambolis, A.; Matralis, H.; Trovarelli, A.; Papadopoulou, Ch. *Appl. Catal., A* **2010**, *377*, 16.
(45) Li, X. K.; Ji, W. J.; Zhao, J.; Wang, S. J.; Au, C. T. *J. Catal.* **2005**, *236*, 181.
(46) Zhang, Z. L.; Tsipouriari, V. A.; Efstathiou, A. M.; Verykios, X. E. *J. Catal.* **1996**, *158*, 51.

(47) Wang, Y. H.; Liu, H. M.; Xu, B. Q. *J. Mol. Catal. A* **2009**, *299*, 44.
(48) Pompeo, F.; Nichio, N. N.; Souza, M. M. V. M; Cesar, D. V.; Ferretti, O. A.; Schmal, M. *Appl. Catal., A* **2007**, No. 316, 175.
(49) Akpan, E.; Sun, Y.; Kumar, P.; Ibrahim, H.; Aboudheir, A.; Idem, R. *Chem. Eng. Sci.* **2007**, *62*, 4012.
(50) Bradford, M. C. J.; Vannice, M. A. *Catal. Rev.−Sci. Eng.* **1999**, *41*, 1.
(51) Nguyen, S. V.; Szabo, V.; Trong, On, D.; Kaliaguine, S. *Microporous Mesoporous Mater.* **2002**, *54*, 51.
(52) Yi, N.; Cao, Y.; Su, Y.; Dai, W. L.; He, H. Y.; Fan, K. N. *J. Catal.* **2005**, *230*, 249.
(53) Wang, N.; Chu, W.; Zhang, T.; Zhao, X. S. *Int. J. Hydrogen Energy* **2012**, *37*, 19.
(54) Xu, L.; Song, H.; Chou, L. *Appl. Catal., B* **2011**, *108−109*, 177.
(55) Therdthianwong, S.; Siangchin, C.; Therdthianwong, A. *Fuel Process. Technol.* **2008**, *89*, 160.
(56) Chen, X.; Honda, K.; Zhang, Z. G. *Appl. Catal., A* **2005**, *288*, 86.
(57) Rezaei, M.; Alavi, S. M.; Sahebdelfar, S.; Bai, P.; Liu, X.; Yan, Z. F. *Appl. Catal., B* **2008**, *77*, 346.
(58) Zhang, W. D.; Liu, B. S.; Zhu, C.; Tian, Y. L. *Appl. Catal., A* **2005**, *292*, 138.
(59) Palmqvist, A. E. C.; Wirde, M.; Gelius, U.; Muhammed, M. *Nanostruct. Mater.* **1999**, *11*, 995.
(60) Wang, H.; Ye, J. L.; Liu, Y.; Li, Y. D.; Qin, Y. N. *Catal. Today* **2007**, *129*, 305.
(61) Chen, S. Q.; Wang, H.; Liu, Y. *Int. J. Hydrogen Energy* **2009**, *34*, 7995.
(62) Baker, R. T. K.; Harris, P. S.; Thomas, R. B.; Waite, R. J. *J. Catal.* **1973**, *30*, 86.
(63) An, L.; Dong, C.; Yang, Y.; Zhang, J.; He, L. *Renew. Energy* **2011**, *36*, 930.
(64) Daza, C. E.; Cabrera, C. R.; Moreno, S.; Molina, R. *Appl. Catal., A* **2010**, *378*, 125.
(65) Yang, R.; Xing, C.; Lv, C.; Shi, L.; Tsubaki, N. *Appl. Catal., A* **2010**, *385*, 92.